

Implementation of the Carr-Purcell-Meiboom-Gill (CPMG) Sequence for Spin Manipulation of Nitrogen Vacancy Centers

Bachelorarbeit

zur Erlangung des akademischen Grades
Bachelor of Science (B. Sc.)



Mathematisch-Naturwissenschaftliche Fakultät
Institut für Physik
Humboldt-Universität zu Berlin

Fabian Loth

geboren am 13.02.1993 in Flensburg

Betreuung: Prof Dr. Oliver Benson
Prof Dr. Kurt Busch

Eingereicht am: 22.02.2016

Abstract

In this thesis, the implementation of the Carr-Purcell-Meiboom-Gill (CPMG) sequence for spin manipulation of single nitrogen vacancy (NV) centers in nano diamond is described.

The theoretical part covers optical and spin properties of NV centers, single photon statistics and the dynamic of a two level quantum system interacting with an electromagnetic wave. Finally the effect of the CPMG sequence on the spin state of an NV center is illustrated.

The experiment begins with methods to find a single NV center and ends with coherent spin manipulation including the CPMG sequence. Thereby the coherence time of the NV center can be measured and prolonged by increasing the number of control pulses.

Zusammenfassung

In dieser Arbeit wird die Implementierung der Carr-Purcell-Meiboom-Gill-Sequenz (CPMG-Sequenz) für Spin-Manipulation von einzelnen Stickstoff-Fehlstellen-Zentren (NV-Zentren) in Nanodiamanten beschrieben.

Der theoretische Teil umfasst optische und Spineigenschaften von NV-Zentren, Einzelphotonenstatistik und die Dynamik eines Zwei-Niveau-Systems in Wechselwirkung mit einer elektromagnetischen Welle. Schließlich wird die Auswirkung der CPMG-Sequenz auf den Spin-Zustand eines NV-Zentrums dargestellt.

Das Experiment beginnt mit Methoden, um ein einzelnes NV-Zentrum zu finden und endet mit kohärenten Spin-Manipulationen, einschließlich der CPMG-Sequenz. Mit dieser kann die Kohärenzzeit des NV-Zentrums gemessen und durch Erhöhung der Anzahl der Kontrollpulse verlängert werden.

Contents

1	Introduction	1
2	Theory	3
2.1	Nitrogen Vacancy Centers in Nano Diamond	3
2.2	Single Photon Statistics	5
2.3	Two Level Quantum System	6
2.3.1	Optical Bloch Equations	7
2.3.2	Rabi Oscillations	11
2.3.3	Bloch Vector	12
2.4	CPMG Sequence	14
3	Experiment	17
3.1	Setup and Sample	17
3.2	Confocal Laser Scanning Microscopy	19
3.3	Hanbury Brown and Twiss Experiment	20
3.4	Optically Detected Magnetic Resonance	20
3.5	Timing of the Sequences	21
3.6	Coherent Spin Manipulation	25
3.6.1	Rabi Oscillations	26
3.6.2	CPMG Experiment	27
4	Conclusion and Outlook	28
A	List of Devices	30
B	List of Abbreviations	31
	References	32

1 Introduction

The nitrogen vacancy (NV) center emerged as a unique object for a variety of applications in quantum optics. It is a point defect in diamond that shows fluorescence. Since excitation and subsequent decay to the initial state takes a finite time, only one photon is emitted at a time. Thus the NV center behaves as a *single photon source*. Because it is a stable solid state system it shows this behaviour without photobleaching and even at room temperature [1].

The most fascinating aspect, however, is the spin-dependence of the fluorescence. The ground and excited state of the NV center are spin triplet in which the $m_s = \pm 1$ states are degenerated and the $m_s = 0$ state is energetically lower. The fluorescence intensity is higher for the “bright” $m_s = 0$ state than for the “dark” $m_s = \pm 1$ states. The spin state of this effective two level quantum system can be manipulated by a resonant electromagnetic field and read out optically by the spin-dependent fluorescence. This method, called optically detected magnetic resonance (ODMR), was first performed on NV centers by A. Gruber et al. [2] and is described in section 3.4.

The NV center as a two level quantum system, which can be manipulated and read out, is one of the most promising realizations of a quantum bit for *quantum information processing* (QIP). While the state of a classic bit is either zero or one, the state of a qubit can be any quantum superposition of the two states. With quantum computing certain mathematical problems, like factorization of integers or quantum simulation, can be solved much faster compared to conventional computers [3]. The first quantum registers containing several qubits based on NV centers were demonstrated [4, 5].

Another application of the NV center is the *nanoscale electric and magnetic sensing*. Since the electron spin of the NV center interacts with electric and magnetic fields, it can be used as a nanoscale sensor [6–10]. Because of the low cytotoxicity [11], nano diamonds containing NV centers can be used in life sciences.

A key factor for both, QIP and sensing, is a long coherence time of the system. Every quantum system underlies decoherence due to interactions with the environment. Techniques to suppress decoherence by decoupling from the environment are called dynamical decoupling (DD). A very effective DD protocol is the Carr-Purcell-Meiboom-Gill (CPMG) sequence. It consists of successive pulses of resonant coherent electromagnetic radiation. With this method the coherence time can be measured and prolonged by increasing the

number of pulses.

The goal of this work is the implementation of the CPMG sequence for spin manipulation of NV centers in nano diamond in order to measure and prolong the coherence time.

An essential requirement for this experiment is an exact timing of spin manipulation, optical excitation and photon detection. During the course of this work systematic methods for the timing have been developed (section 3.5).

2 Theory

This chapter covers the fundamental theory for the experiments described in chapter 3.

First, the NV center with its special optical and spin properties is illustrated with the help of an energy level diagram.

Second, single photon statistics are explained with the concept of the quantum-mechanical degree of second-order coherence.

Third, the theory of a two-level quantum system interacting with an electromagnetic wave is investigated. The dynamic is derived starting from the Schrödinger equation and resulting in the optical Bloch equations. Their solutions lead to the Rabi oscillations. The Bloch vector, a representation of the state of a two level quantum system, is introduced for visualization.

Finally, the CPMG sequence is explained with the Bloch vector representation.

2.1 Nitrogen Vacancy Centers in Nano Diamond

Diamond is a crystal consisting of carbon atoms in a face centred cubic (fcc) lattice with a two atom basis $\{(0, 0, 0), (\frac{1}{4}, \frac{1}{4}, \frac{1}{4})\}$ and a lattice constant of 3.56 \AA [12]. With a band gap of 5.5 eV , diamond is optically transparent [12]. A nitrogen vacancy center is a point defect in the diamond lattice which acts as a color center that absorbs and emits light in the visible spectrum. It consists of a nearest neighbour pair of a nitrogen atom, which substitutes for a carbon atom, and a lattice vacancy. It occurs in a neutral (NV^0) state and a negatively charged state (NV^-). For spin manipulation only the NV^- center is suitable and in the following it will simply be referred to as NV center. The following general information about NV centers are taken from Ref. [13]. The electronic structure of the NV center involves six electrons. Two are provided by the nitrogen atom, another three are dangling bonds from the three carbon atoms surrounding the vacancy and the sixth electron is captured from the lattice.

A simple energy level diagram of the NV center is shown in Fig. 1. It consists of three electronic levels, including a ground state $|g\rangle$, an excited state $|e\rangle$ and a metastable singlet state $|s\rangle$. The main transition from $|e\rangle$ to $|g\rangle$ is radiative with a resonant wavelength of 638 nm (zero phonon line) (Fig. 2), whereas the transitions from $|e\rangle$ to $|s\rangle$ and from $|s\rangle$ to $|g\rangle$ are non-radiative. Ground and excited state are spin triplet ($m_s = -1, 0, +1$) and further split

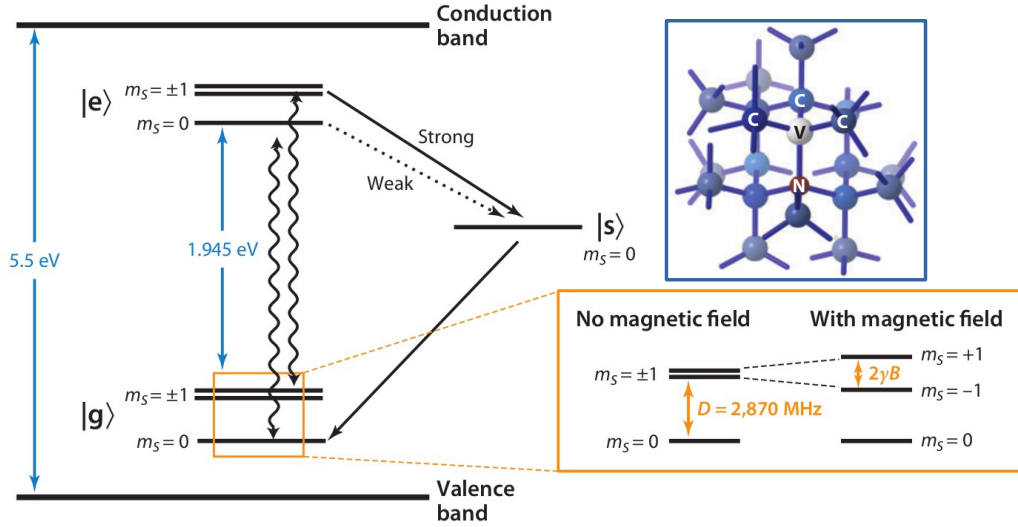


Figure 1: (left) Energy level diagram of the NV center consisting of a ground state $|g\rangle$, an excited state $|e\rangle$ and a metastable singlet state $|s\rangle$. (right bottom) The three spin sublevels with $m_s = 0$ and $m_s = \pm 1$. D is the zero-field splitting and $2\gamma B$ is the Zeeman splitting, where γ is the electron gyromagnetic ratio and B the magnetic field. (right top) Lattice structure of the NV center with one nitrogen atom N and three carbon atoms C surrounding the vacancy V. Taken from Ref. [13].

into three sublevels. The $m_s = \pm 1$ states are degenerated and the $m_s = 0$ state is energetically lower. The energy difference between spin sublevels is $D = 2.87 \text{ GHz}$ for the ground state and $D = 1.42 \text{ GHz}$ for the excited state, where D is the so-called zero-field splitting. With an external magnetic field the degeneracy is lifted because of the Zeeman effect. Optical transitions are strongly spin preserving, meaning that the spin state does not change while cycling between $|g\rangle$ and $|e\rangle$. The non-radiative transitions from $|e\rangle$ to $|s\rangle$ state have a higher probability for the $|e, m_s = \pm 1\rangle$ state (continuous arrow) than for the $|e, m_s = 0\rangle$ state (dashed arrow). This leads to an optical contrast between the "bright" $m_s = 0$ state and the "dark" $m_s = \pm 1$ state of approximately 30 %. The optical contrast is only temporary and disappears for long laser illumination, as decay via the $|s\rangle$ singlet state always repumps the electron to $m_s = 0$. This contrast is the basis for optically detected magnetic resonance (ODMR) as described in section 3.4.

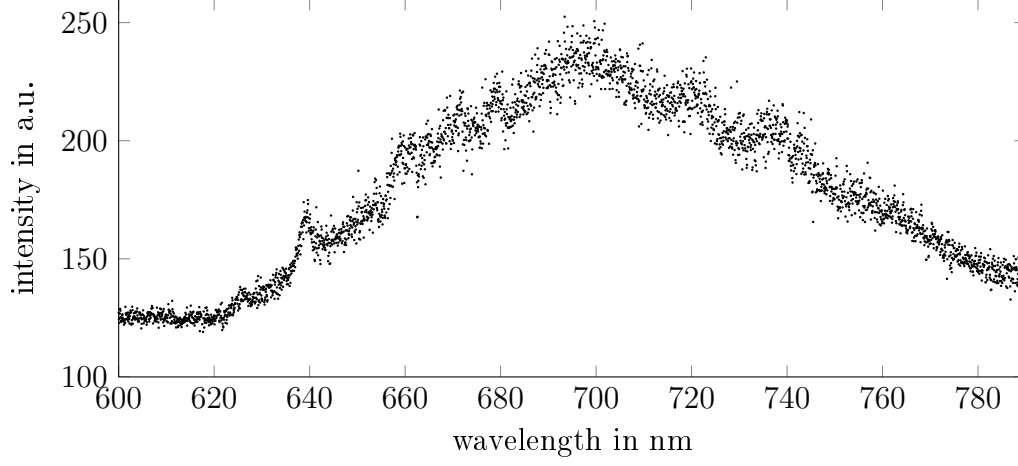


Figure 2: Fluorescence spectrum of an NV center at room temperature with the zero phonon line (ZPL) at 638 nm and the phonon side band from 650 nm to 790 nm.

2.2 Single Photon Statistics

This section covers the theoretic background to identify NV centers by their behaviour as a single photon emitter. It is based on the quantum-mechanical degree of second-order coherence $g^{(2)}$, which is evaluated for a Fock state following Ref. [14]. In general $g^{(2)}$ describes the intensity coherence of two space-time points and is defined as

$$g^{(2)}(\mathbf{r}_1, t_1, \mathbf{r}_2, t_2) = \frac{\langle \hat{E}^-(\mathbf{r}_1, t_1) \hat{E}^-(\mathbf{r}_2, t_2) \hat{E}^+(\mathbf{r}_2, t_2) \hat{E}^+(\mathbf{r}_1, t_1) \rangle}{\langle \hat{E}^-(\mathbf{r}_1, t_1) \hat{E}^+(\mathbf{r}_1, t_1) \rangle \langle \hat{E}^-(\mathbf{r}_2, t_2) \hat{E}^+(\mathbf{r}_2, t_2) \rangle}. \quad (1)$$

Here, \hat{E}^- and \hat{E}^+ are the electric field operators

$$\hat{E}^-(\mathbf{r}, t) \propto \hat{a}^\dagger(\mathbf{r}, t) e^{-i(\mathbf{k} \cdot \mathbf{r} - \omega t)}, \quad \hat{E}^+(\mathbf{r}, t) \propto \hat{a}(\mathbf{r}, t) e^{i(\mathbf{k} \cdot \mathbf{r} - \omega t)} \quad (2)$$

with \hat{a}^\dagger and \hat{a} being the creation and annihilation operators. For parallel light the definition of $g^{(2)}$ simplifies by the replacement of \mathbf{r} by z . The space-time coordinates enter the coherence only in form of the delay time

$$\tau = t_2 - t_1 - \frac{z_2 - z_1}{c}, \quad (3)$$

where c is the speed of light. For a stationary light beam, which means that the statistical properties are time independent, $g^{(2)}$ reduces to

$$g^{(2)}(\tau) = \frac{\langle \hat{E}^-(t) \hat{E}^-(t+\tau) \hat{E}^+(t+\tau) \hat{E}^+(t) \rangle}{\langle \hat{E}^-(t) \hat{E}^+(t) \rangle^2}. \quad (4)$$

Substitution of eq. 2 into eq. 4 gives

$$g^{(2)}(\tau) = \frac{\langle \hat{a}^\dagger(t) \hat{a}^\dagger(t+\tau) \hat{a}(t+\tau) \hat{a}(t) \rangle}{\langle \hat{a}^\dagger(t) \hat{a}(t) \rangle^2}. \quad (5)$$

To distinguish between different light sources the coherence at zero time delay $g^{(2)}(0)$ is investigated. In this case all operators act at the same time t so that the time dependence can be left out

$$g^{(2)}(0) = \frac{\langle \hat{a}^\dagger \hat{a}^\dagger \hat{a} \hat{a} \rangle}{\langle \hat{a}^\dagger \hat{a} \rangle^2}. \quad (6)$$

Laser light for instance can be described by coherent states which are eigenstates of the annihilation operator so that one can simply calculate $g^{(2)}(0) = 1$. However, light of a single photon emitter can be described by a Fock state, or number state, which is an eigenstate of the number operator $\hat{n} = \hat{a}^\dagger \hat{a}$. The eigenvalue n is the number of photons in this state. With the commutator relation $[\hat{a}, \hat{a}^\dagger] = 1$ the correlation function becomes

$$g^2(0) = \frac{\langle \hat{a}^\dagger (\hat{a} \hat{a}^\dagger - 1) \hat{a} \rangle}{\langle \hat{a}^\dagger \hat{a} \rangle^2} = \frac{\langle \hat{n} \hat{n} \rangle - \langle \hat{n} \rangle}{\langle \hat{n} \rangle^2} = 1 - \frac{1}{n}. \quad (7)$$

It can be measured with a *Hanbury Brown and Twiss* interferometer, which is described in section 3.3.

2.3 Two Level Quantum System

The theory of a two level quantum system interacting with an electromagnetic field is the basis for the experiments described in this thesis. The corresponding equations of motion, the optical Bloch equations (OBEs), are derived starting from the Schrödinger equation. The solutions of the OBEs lead to the Rabi oscillations. A graphical representation of the two level

quantum system is introduced with the Bloch vector.

In the experiment the two level system consists of the $m_s = 0$ state and one of the $m_s = \pm 1$ states (their degeneracy is lifted by an external magnetic field), which correspond in the following to $|0\rangle$ and $|1\rangle$ respectively.

2.3.1 Optical Bloch Equations

In this section the dynamic for a two level quantum system interacting with an electromagnetic field is derived following Ref. [14,15]. The theory is based on the time-dependent *Schrödinger equation*

$$\hat{H} |\Psi(\mathbf{r}, t)\rangle = i\hbar \frac{\partial |\Psi(\mathbf{r}, t)\rangle}{\partial t}, \quad (8)$$

where \hat{H} is the generally time-dependent Hamiltonian and $|\Psi(\mathbf{r}, t)\rangle$ the time-dependent wave function. For a system without external radiation field, the Hamiltonian \hat{H}_0 is time-independent and eq. 8 has solutions of the form

$$|\Psi_n(\mathbf{r}, t)\rangle = |\psi_n(\mathbf{r})\rangle e^{-i\omega_n t}. \quad (9)$$

Substitution of eq. 9 into eq. 8 produces the energy eigenvalue equation

$$\hat{H}_0 |\psi_n(\mathbf{r})\rangle = E_n |\psi_n(\mathbf{r})\rangle. \quad (10)$$

The interaction with the radiation field is described by an additional interaction Hamiltonian $\hat{H}_I(t)$ that is explicitly time-dependent

$$\hat{H}(t) = \hat{H}_0 + \hat{H}_I(t). \quad (11)$$

The solution of the Schrödinger equation for the total Hamiltonian \hat{H} can be expanded in terms of the eigenfunctions $|\psi_n(\mathbf{r})\rangle$, because they form a complete set

$$|\Psi(\mathbf{r}, t)\rangle = \sum_k c_k(t) |\psi_k(\mathbf{r})\rangle e^{-i\omega_k t}. \quad (12)$$

The complex coefficients $c_k(t)$ are generally time-dependent. Substitution of eq. 11 and 12 into eq. 8 gives

$$\left(\hat{H}_0 + \hat{H}_I(t) \right) \sum_k c_k(t) |\psi_k(\mathbf{r})\rangle e^{-i\omega_k t} = i\hbar \frac{\partial}{\partial t} \sum_k c_k(t) |\psi_k(\mathbf{r})\rangle e^{-i\omega_k t}. \quad (13)$$

Multiplying by $\langle \psi_j(\mathbf{r}) |$ gives

$$\sum_k c_k(t) \langle \psi_j(\mathbf{r}) | \hat{H}_I(t) | \psi_k(\mathbf{r}) \rangle e^{i(\omega_j - \omega_k)t} = i\hbar \frac{dc_j(t)}{dt}. \quad (14)$$

This general equation will be further investigated for the special case of a two level system consisting of a ground state $|0\rangle$ and an excited state $|1\rangle$ with the energies $E_0 = \hbar\omega_0$ and $E_1 = \hbar\omega_1$ and the transition frequency $\omega_{10} = \omega_1 - \omega_0$. In the following the time dependencies are not denoted and time derivatives are indicated with a dot. Eq. 14 simplifies to the following equations for the two coefficients c_0 and c_1

$$\langle 0 | \hat{H}_I | 0 \rangle c_0 + e^{-i\omega_{10}t} \langle 0 | \hat{H}_I | 1 \rangle c_1 = i\hbar \cdot \dot{c}_0, \quad (15)$$

$$e^{i\omega_{10}t} \langle 1 | \hat{H}_I | 0 \rangle c_0 + \langle 1 | \hat{H}_I | 1 \rangle c_1 = i\hbar \cdot \dot{c}_1. \quad (16)$$

To evaluate the brackets in eq. 15 and 16 the form of the interaction Hamiltonian is investigated. The atom (or NV center) consists of a nucleus of charge Ze surrounded by Z electrons each of charge $-e$. It interacts with an electromagnetic wave given by

$$\mathbf{E} = \mathbf{E}_0 \cos(\mathbf{k} \cdot \mathbf{r} - \omega t), \quad \mathbf{B} = \mathbf{B}_0 \cos(\mathbf{k} \cdot \mathbf{r} - \omega t). \quad (17)$$

Since the radius of the atom is much smaller than the typical wavelength of an applied electromagnetic wave the spatial variation of the electromagnetic field is negligible. Then it is a good approximation to put $\mathbf{r} = 0$. The total electric dipole moment of the atom is

$$\mathbf{d} = -e \sum_i^Z \mathbf{r}_i, \quad (18)$$

where \mathbf{r}_i are the coordinates of the electrons and the coordinate of the nucleus is set to zero. The main contribution to the interaction Hamiltonian comes from the potential energy of this electric dipole in the electric field of the light beam. In this so-called *electric dipole approximation* the interaction Hamiltonian becomes

$$\hat{H}_I = \mathbf{d} \cdot \mathbf{E} = \mathbf{d} \cdot \mathbf{E}_0 \cos(\omega t). \quad (19)$$

The dipole moment is in general difficult to calculate but the following properties of the matrix elements can be derived considering parity. The interaction Hamiltonian is real and has odd parity, which means that it changes sign under inversion of the spatial coordinate ($\mathbf{r}_i \rightarrow -\mathbf{r}_i$). The diagonal matrix elements have even parity, because the integrand is a product of two wave functions with the same parity, and must therefore vanish

$$\langle 0|\hat{H}_I|0\rangle = \int dV \psi_0^* \hat{H}_I \psi_0 = 0, \quad \langle 1|\hat{H}_I|1\rangle = \int dV \psi_1^* \hat{H}_I \psi_1 = 0. \quad (20)$$

Because of the selection rule an electric dipole transition can only occur if the two states have different parity. Providing that, the off-diagonal elements are related by

$$\langle 1|\hat{H}_I|0\rangle = \langle 0|\hat{H}_I|1\rangle. \quad (21)$$

With the definition of the Rabi frequency

$$\Omega = \frac{\mathbf{d}_{10} \cdot \mathbf{E}_0}{\hbar}, \quad (22)$$

where $\mathbf{d}_{10} = \langle 1|\mathbf{d}|0\rangle$ is the transition dipole moment, the off-diagonal elements can be written as

$$\langle 1|\hat{H}_I|0\rangle = \langle 0|\hat{H}_I|1\rangle = \hbar\Omega \cos(\omega t). \quad (23)$$

Inserting eq. 23 into eq. 15 and 16 gives

$$\dot{c}_0 = -i\Omega \cos(\omega t) e^{-i\omega_{10}t} c_1, \quad (24)$$

$$\dot{c}_1 = -i\Omega \cos(\omega t) e^{i\omega_{10}t} c_0. \quad (25)$$

Since only the bilinear products of the coefficients are observable, it is convenient to continue with the density matrix elements defined by

$$\rho_{00} = c_0 c_0^*, \quad \rho_{11} = c_1 c_1^*, \quad \rho_{01} = c_0 c_1^*, \quad \rho_{10} = c_1 c_0^*. \quad (26)$$

The off-diagonal elements, or *coherences*, are generally complex but the diagonal elements, or *populations* are real and because of the normalization they satisfy $\rho_{00} + \rho_{11} = 1$. The equations of motion for the density matrix

elements can be found from eq. 24 and 25

$$\dot{\rho}_{11} = -\dot{\rho}_{00} = -i\Omega \cos(\omega t) (e^{i\omega_{10}t} \rho_{01} - e^{-i\omega_{10}t} \rho_{10}), \quad (27)$$

$$\dot{\rho}_{01} = \dot{\rho}_{10}^* = i\Omega \cos(\omega t) e^{-i\omega_{10}t} (\rho_{00} - \rho_{11}). \quad (28)$$

This can be simplified with the *rotating wave approximation* (RWA). For this it's useful to write $\cos(\omega t) = \frac{1}{2}(e^{i\omega t} + e^{-i\omega t})$. The effect of terms that oscillate at frequency $\omega_{10} + \omega$ are negligible compared to terms that oscillate at frequency $\omega_{10} - \omega$. Removal of fast oscillating terms produces the equations of motion

$$\dot{\rho}_{11} = -\dot{\rho}_{00} = -\frac{1}{2}i\Omega (e^{-i(\omega_{10}-\omega)t} \rho_{01} - e^{i(\omega_{10}-\omega)t} \rho_{10}), \quad (29)$$

$$\dot{\rho}_{01} = \dot{\rho}_{10}^* = \frac{1}{2}i\Omega e^{-i(\omega_{10}-\omega)t} (\rho_{00} - \rho_{11}). \quad (30)$$

These equations are known as the *optical Bloch equations* (OBEs). By introducing the detuning $\Delta = \omega_{10} - \omega$ and the substitutions

$$\tilde{\rho}_{01} = e^{i\Delta t} \rho_{01}, \quad \tilde{\rho}_{10} = e^{-i\Delta t} \rho_{10} \quad (31)$$

this can be further simplified to

$$\dot{\rho}_{11} = -\dot{\rho}_{00} = -\frac{1}{2}i\Omega (\tilde{\rho}_{01} - \tilde{\rho}_{10}), \quad (32)$$

$$\dot{\tilde{\rho}}_{01} = \dot{\tilde{\rho}}_{10}^* = \frac{1}{2}i\Omega (\rho_{00} - \rho_{11}) + i\Delta \tilde{\rho}_{01}. \quad (33)$$

Up to this point it is not considered that the system can spontaneously relax from $|1\rangle$ to $|0\rangle$. This effect of spontaneous emission is introduced in a phenomenological way. The optical Bloch equations are modified with one decay rate for the populations γ_1 and one for the coherences γ_2

$$\dot{\rho}_{11} = -\dot{\rho}_{00} = -\frac{1}{2}i\Omega (\tilde{\rho}_{01} - \tilde{\rho}_{10}) - \gamma_1 \rho_{11}, \quad (34)$$

$$\dot{\tilde{\rho}}_{01} = \dot{\tilde{\rho}}_{10}^* = \frac{1}{2}i\Omega (\tilde{\rho}_{00} - \tilde{\rho}_{11}) + (i\Delta - \gamma_2) \tilde{\rho}_{01}. \quad (35)$$

The inverse of the decay rates are called the longitudinal (or spin-lattice) relaxation time $T_1 = 1/\gamma_1$ and the transverse (or spin-spin) relaxation time $T_2 = 1/\gamma_2$. T_1 corresponds to the life time of the excited state and T_2 to the coherence of the system. Dephasing can be taken into account by adding a dephasing rate to the decoherence rate γ_2 . The modified decoherence rate is

named γ_2^* and the corresponding time is $T_2^* = 1/\gamma_2^*$. For the three times it is $2T_1 \geq T_2 \geq T_2^*$ [16]. Next, the solutions of the OBEs are discussed.

2.3.2 Rabi Oscillations

The analytical solution of the OBEs (eq. 34 and 35), including detuning Δ and damping caused by spontaneous, given by the two relaxation times fulfilling $2T_1 \geq T_2$, was first found by H. C. Torrey [17] and is also described in Ref. [18].

Because this approach is quite complicated the following discussion is restricted to two simplifying cases following Ref. [14].

The first case includes detuning Δ but no damping $\gamma_1 = \gamma_2 = 0$. For the initial conditions $\rho_{11} = \tilde{\rho}_{01} = 0$ the populations are given by

$$\rho_{11}(t) = (\Omega/\Omega')^2 \sin^2\left(\frac{1}{2}\Omega't\right), \quad (36)$$

where the generalized Rabi frequency $\Omega' = \sqrt{\Omega^2 + \Delta^2}$ was introduced. The result is shown in Fig. 3 for different values of detuning. Detuning increases the frequency but decreases the amplitude.

The second case includes damping, given by dependent relaxation times $2T_1 = T_2 = T_2^*$, but no detuning $\Delta = 0$. For the same initial conditions as before the populations become

$$\rho_{11}(t) = \underbrace{\left(\frac{\frac{1}{2}\Omega^2}{2\gamma_2^2 + \Omega^2}\right)}_{\rho_{11}(\infty)} \left(1 - \left(\cos(\lambda t) + \frac{3\gamma_2}{2\lambda} \sin(\lambda t)\right) \exp\left(-\frac{3\gamma_2 t}{2}\right)\right) \quad (37)$$

with $\lambda = \sqrt{\Omega^2 - \gamma_2^2}/4$. The result is shown in Fig. 3 for different values of damping. The population is oscillating with frequency λ and is damped to $\rho_{11}(\infty)$.

In the case of no detuning and no damping eq. 36 and 37 both reduce to

$$\rho_{11}(t) = \sin^2\left(\frac{1}{2}\Omega t\right). \quad (38)$$

The result corresponds to the blue lines in Fig. 3.

A resonant electromagnetic pulse of the length $t = \pi/\Omega$, called π pulse, exactly inverts the populations.

In the following, the Bloch sphere is introduced to visualize the dynamic of

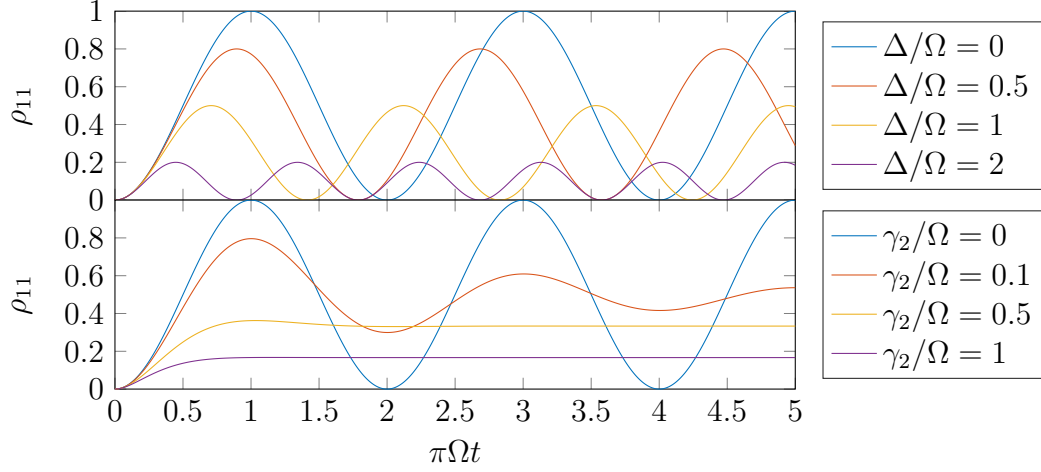


Figure 3: *Rabi oscillations* (top) for different values of detuning Δ in the case of no damping $\gamma_1 = \gamma_2 = 0$ and (bottom) for different values of damping γ_2 with $\gamma_2 = \frac{1}{2}\gamma_1$ in the case of resonant excitation $\Delta = 0$.

a two-level quantum system.

2.3.3 Bloch Vector

The Bloch vector is a representation of a pure state of a two-level quantum system. In quantum computing such a system is called a quantum bit, or *qubit* for short. Any pure state $|\psi\rangle$ can be written as a linear combination of the basis states $|0\rangle$ and $|1\rangle$

$$|\psi\rangle = c_0 |0\rangle + c_1 |1\rangle. \quad (39)$$

Because of normalization the complex coefficients fulfill $|c_0|^2 + |c_1|^2 = 1$ and the wave function may be rewritten as [3]

$$|\psi\rangle = e^{i\gamma} \left(\cos \frac{\theta}{2} |0\rangle + e^{i\varphi} \sin \frac{\theta}{2} |1\rangle \right), \quad (40)$$

where θ, φ, γ are real coefficients. Since only relative phases are observable the factor $e^{i\gamma}$ can be left out and it remains

$$|\psi\rangle = \cos \frac{\theta}{2} |0\rangle + (\cos \varphi + i \sin \varphi) \sin \frac{\theta}{2} |1\rangle. \quad (41)$$

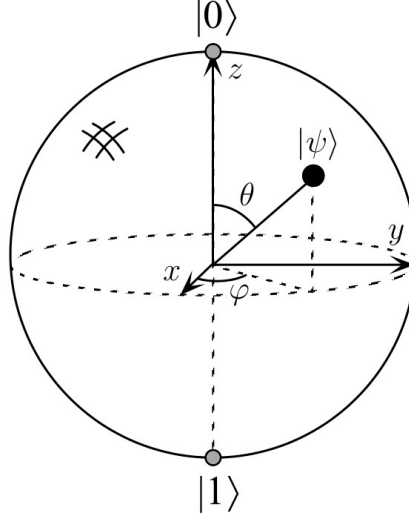


Figure 4: Bloch sphere representation of a two state quantum system (qubit). Taken from Ref. [3].

With θ and φ being spherical coordinates the *Bloch vector*

$$\begin{pmatrix} x \\ y \\ z \end{pmatrix} = \begin{pmatrix} \sin \theta \cos \varphi \\ \sin \theta \sin \varphi \\ \cos \theta \end{pmatrix} \quad (42)$$

defines a point on the unit three-dimensional sphere, the so-called *Bloch sphere* (Fig. 4). The two states $|0\rangle$ and $|1\rangle$ correspond to the poles.

The Bloch vector can also be expressed with the density matrix elements. For the system which is described by the wave function in eq. 41 the diagonal elements are given by

$$\rho_{00} = c_0 c_0^* = \cos^2 \frac{\theta}{2}, \quad \rho_{11} = c_1 c_1^* = \sin^2 \frac{\theta}{2}. \quad (43)$$

And with $\cos \frac{\theta}{2} \sin \frac{\theta}{2} = \frac{1}{2} \sin \theta$ the off-diagonal elements become

$$\rho_{01} = \rho_{10}^* = c_0 c_1^* = \frac{1}{2} \sin \theta (\cos \varphi - i \sin \varphi). \quad (44)$$

It can be shown that the Bloch vector written with the density matrix elements is

$$\begin{pmatrix} x \\ y \\ z \end{pmatrix} = \begin{pmatrix} \rho_{01} + \rho_{10} \\ i(\rho_{01} - \rho_{10}) \\ \rho_{00} - \rho_{11} \end{pmatrix} = \begin{pmatrix} c_0 c_1^* + c_1 c_0^* \\ i(c_0 c_1^* - c_1 c_0^*) \\ |c_0|^2 - |c_1|^2 \end{pmatrix}, \quad (45)$$

where $\cos^2 \frac{\theta}{2} - \sin^2 \frac{\theta}{2} = \cos \theta$ was used for the z component. The behaviour of a two level system interacting with a resonant electromagnetic field with frequency ω can be described best on a Bloch sphere rotating with this frequency. Starting from $|0\rangle$, resonant Rabi oscillations change the polar angle θ and dephasing results in a change of the azimuthal angle φ . In the following, the Bloch sphere representation is used to describe the CPMG sequence.

2.4 CPMG Sequence

The CPMG sequence is a method to measure the coherence time T_2 . It consists of coherent pulses of resonant electromagnetic radiation. For spin manipulation of NV centers the resonance frequency is given by the splitting of the $m_s = 0$ and one of the $m_s = \pm 1$ ground states. The sequence is explained on the Bloch sphere, rotating with this frequency around the z axis, where $|0\rangle$ corresponds to the $m_s = 0$ state and $|1\rangle$ to one of the $m_s = \pm 1$ states.

Fig. 5 shows the Bloch sphere representation and a scheme of the CPMG sequence. After initialization to $|0\rangle$ a $\pi/2$ pulse at time $t = 0$ converts the populations into coherences (a). Due to quantum decoherence the system is prone to dephasing (b). A π pulse at $t = \tau$ inverts the coherences (c). The inversion brings the system to rephasing (d). The process of dephasing-inversion-rephasing is repeated n times, symbolized by the arrow from (d) to (b). All together there are n successive π pulses at $t = (2j - 1)\tau$ with $j = 1, \dots, n$. Finally a $\pi/2$ pulse at $t = 2n\tau$ takes the system back to $|0\rangle$ and the fluorescence can be read out.

The time τ is constant for the complete sequence (a) to (e), but the sequence is repeated while τ is stepwise increased.

The rotation axis (blue arrow) is defined by the phase of the electromagnetic field. For coherent pulses without any relative phase shift the rotation axis would always point in the same direction. The different rotation axes in the CPMG sequence are realized by relatively phase shifted pulses.

In the CPMG sequence all spin echoes point in the same direction and it is

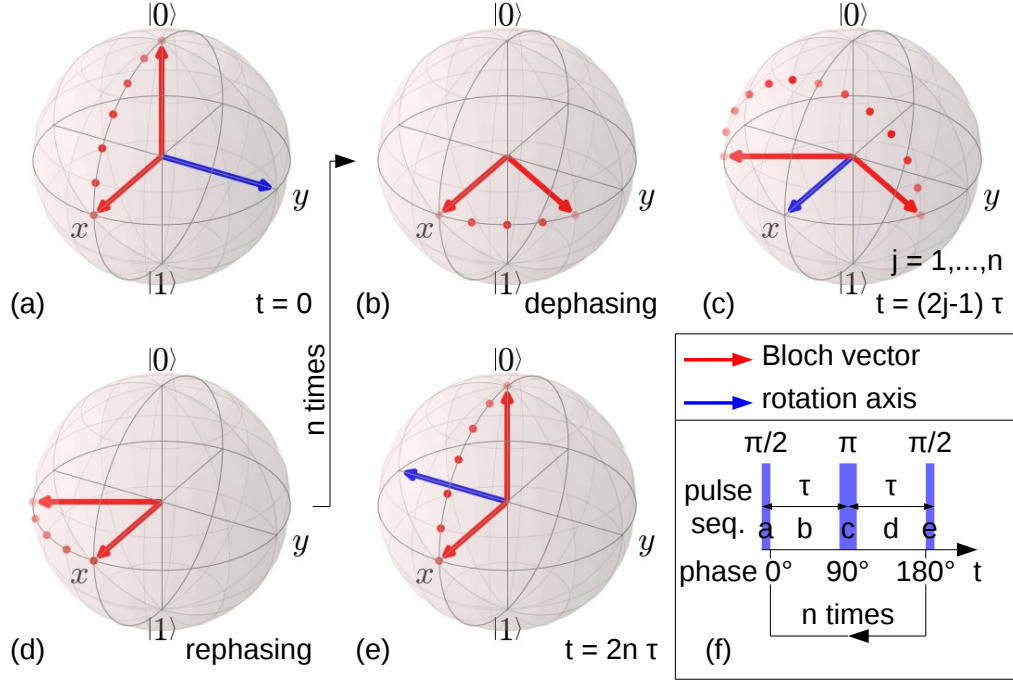


Figure 5: (a) to (e) CPMG sequence represented on the Bloch sphere. (f) Scheme of the CPMG sequence.

robust against deviations of the pulse lengths. If the pulses are for instance somewhat too short, the first $\pi/2$ pulse changes the polar angle to $\theta < \pi/2$ and the π pulses always bring it back to the same θ . The pulse errors do not accumulate.

Spin echoes were first detected in nuclear magnetic resonance (NMR) by E. L. Hahn in 1950 [19] and are sometimes referred to as Hahn echoes. Therefore the CPMG sequence with one π pulse and no phase shift, called Hahn echo sequence, was used. It was extended to many π pulses by H. Y. Carr and E.M. Purcell [20] and modified with the phase shift by S. Meiboom and D. Gill [21].

For spin manipulation of NV centers these sequences are transferred from NMR to electron paramagnetic resonance (EPR), where electron spins are excited instead of the spins of atomic nuclei. The NV centers fluorescence is detected as a function of τ . According to a theoretical model [22] the spin

echo intensity decays as

$$I_{\text{echo}}(\tau) = \exp\left(-\frac{2n\tau}{T_2} \left(\frac{2\tau}{T_2}\right)^2\right). \quad (46)$$

Using his model the coherence time T_2 can be determined. Furthermore the CPMG sequence prolongs the T_2 time compared to the Hahn echo sequence, which was demonstrated for NV centers in Ref. [23].

3 Experiment

This chapter covers the experimental part, which is explained using the theoretic models that were derived in chapter 2.

First, the setup is described with a simplified scheme.

Next, the methods and their results are presented. Confocal microscopy is used to image the sample. NV centers are identified by their behaviour as a single photon emitter in a Hanbury Brown and Twiss interferometer. The EPR frequency is determined by the spin dependent fluorescence with optically detected magnetic resonance. Section 3.5 is a technical part, which describes the timing between different components of the experiment. It is necessary for coherent spin manipulation, including Rabi oscillations and the CPMG sequence. The former gives the Rabi frequency Ω and the latter results in a spin echo decay which gives the coherence time T_2 .

3.1 Setup and Sample

In this section the setup for spin manipulation of single NV centers, ultimately with the CPMG sequence, is explained. It consists of a confocal laser scanning microscope, a Hanbury Brown and Twiss interferometer and a microwave setup. A simplified scheme of the setup is shown in Fig. 6 and a list of devices with the most important properties can be found in appendix A. The focus of my work was the implementation of the CPMG sequence and the integration of the phase shifter.

The sample, a glass cover slip with nano diamonds containing NV centers, is attached to a microwave antenna. The antenna is a gold stripline on a printed circuit board (PCB) with coaxial connectors on both sides and can be moved in all directions with an xyz stage.

The light source is a green 532 nm continuous wave (cw) laser that can be switched fast using an acousto-optic modulator (AOM). The laser power was measured directly in front of the microscope objective to be around 4 mW and the extinction ratio of the AOM is 2000 : 1. The beam is coupled into a single mode fibre (SMF) and then reflected on a dichroic mirror (DM). It can be walked with scanning mirrors (SM) that are moved by piezo elements. The light is focussed on the sample using an oil immersion objective lens with a high numerical aperture of $NA = 1.4$. NV centers that are excited by the laser light emit red fluorescence light that is collected with the same objective. Fluorescence light is transmitted at the DM whereas laser light

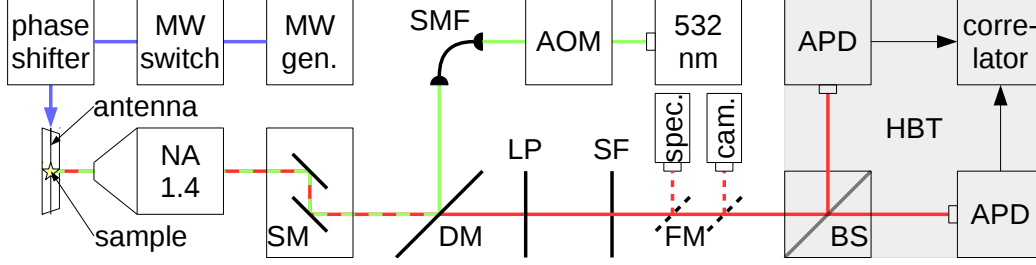


Figure 6: Simplified scheme of the setup consisting of a confocal microscope, an HBT interferometer and a microwave setup for spin manipulation.

is almost completely reflected. A 620 nm long pass filter (LP) filters the remaining laser light. After a spatial filter (SF), which is a 50 μm pinhole in the focal plane of a telescope, the light is directed into the Hanbury Brown and Twiss (HBT) interferometer. Alternatively it can be directed to a camera or a spectrometer using flipping mirrors (FM). In the HBT interferometer the light is split up with a 50:50 beam splitter (BS) and detected with two avalanche photo diodes (APDs). A time correlated single photon counting (TCSPC) correlates the APD signals.

The APD signals can be gated, meaning that the measured signal passes only if the gate is open. There are two gates, the signal (sig) and the reference (ref) gate. The normalized intensity is given by the quotient sig/ref.

For spin manipulation the NV center needs to be in the electromagnetic field of a microwave (MW). The MW frequency and power is set with the MW generator. MW pulses, if necessary relatively phase shifted, are realized with an MW switch and a 6 bit phase shifter with a phase step of $360^\circ/2^6 = 5.625^\circ$. The MW is amplified and sent to the antenna.

A bit pattern generator (BPG) with a timing resolution of 6.7 ns is used to switch MW, phase shifter, AOM and APD gates. The BPG signals are read out with an oscilloscope to monitor the sequence. Signal and reference can be read out with a LabView interface. Controlling the sequence and the scanning is also done with LabView programs.

The investigated nano diamonds are synthetically compounded by Microdiamond AG, Switzerland, called Quantum Particle QP25 and have an average diameter of 25 nm. The nano diamonds are diluted in water and spin-coated onto cover slips.

Therefore the cover slips were cleaned in an ultrasonic water quench with a cleaning concentrate (HellmanexII). After dropping 20 μl of the nano di-

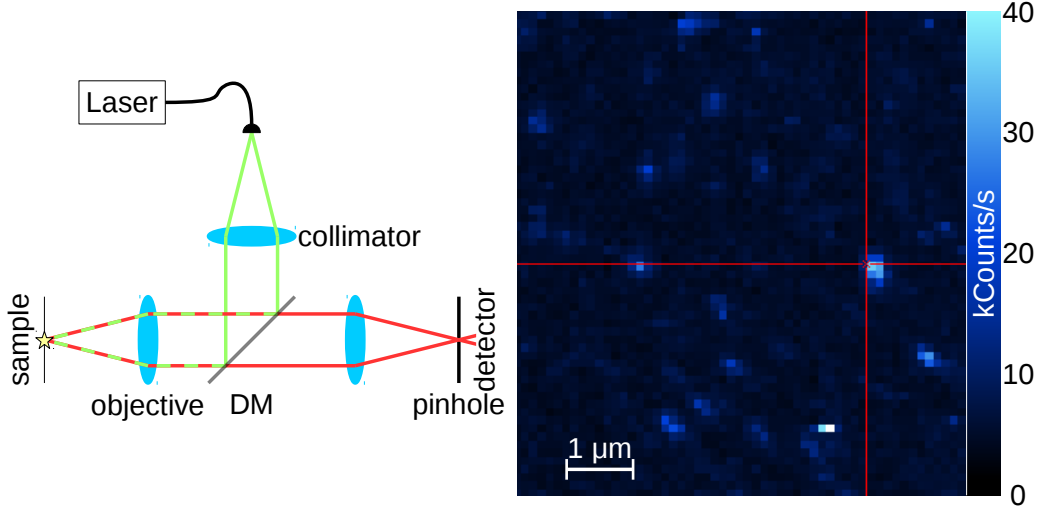


Figure 7: (left) Working principle of the confocal microscope. (right) Typical scan image. The red cross marks the current focus position which is on an NV center.

among dilution onto the cover slip, the spin coater was accelerated within about 10 s up to a maximum frequency of 3 kHz and the total spin coating time was set to 60 s.

3.2 Confocal Laser Scanning Microscopy

The working principle of a confocal microscope is illustrated in Fig. 7. A laser, coupled into a SMF, is used as a point light source. The collimated beam is reflected on a DM and focussed on the sample with an objective lens. Fluorescence light is collected with the same objective lens, passes the DM and is focussed on a pin hole before it is detected. The illumination point in the sample and the point in the middle of the pinhole are confocal. Compared to a usual microscope this principle increases the contrast but has the consequence that only one point at once can be imaged.

To get a complete image of the sample it is scanned. In a confocal laser scanning microscope the laser beam is walked with movable mirrors. A typical scan image is shown in Fig. 7.

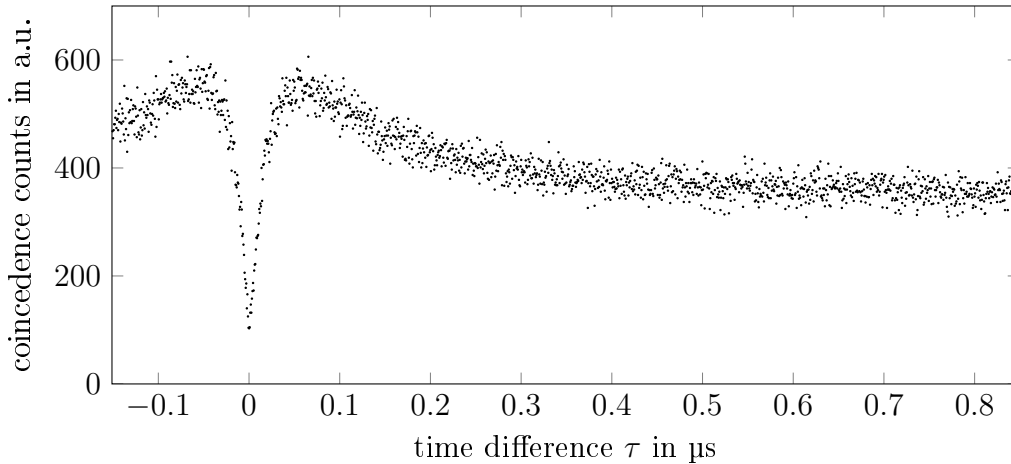


Figure 8: Coincidence measurement for a single NV center. It is proportional to the coherence function $g^{(2)}(\tau)$.

3.3 Hanbury Brown and Twiss Experiment

Single NV centers can be identified by verifying their behaviour as a single photon emitter. In an HBT interferometer the light is split up by a 50:50 beam splitter and detected with two APDs. The correlator starts a time measurement if one APD detects a photon and stops if the other APD detects a photon. An HBT setup measures coincidences of photon detection events. The number of events as a function of the time difference τ is shown in Fig. 8. In the limit of low count rates and short correlation times the result is proportional to the coherence function $g^{(2)}(\tau)$ of the system that was discussed in section 2.2. If the light originates from a single photon emitter, the detectors will never detect one photon each simultaneously and therefore the correlation function at zero time delay $g^{(2)}(0)$ will vanish. This effect is called anti-bunching. But due to background fluorescence and the limited time resolution it will not vanish completely.

3.4 Optically Detected Magnetic Resonance

The spin-dependent fluorescence of the NV center, described in section 2.1, can be used to optically detect the spin state. In an ODMR experiment, the NV center is excited non-resonantly while the MW frequency is scanned over

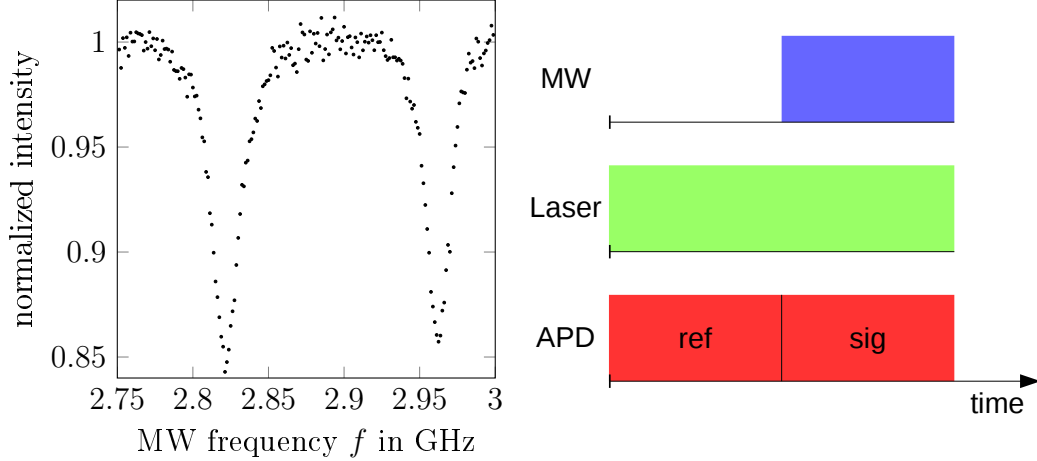


Figure 9: (left) ODMR scan, where the dips correspond to the $m_s = \pm 1$ states. Their degeneracy is lifted with a static magnetic field. The MW power was set to 12 dBm at the MW generator. (right) The corresponding measurement scheme with a length of a 300 μs .

the resonances of the NV centers level splitting between the $m_s = 0$ and the $m_s = \pm 1$ ground states. Fig. 9 shows the fluorescence intensity as a function of the MW frequency and the corresponding measurement scheme. The total duration of the sequence is typically set to a few hundred μs . As the MW frequency is resonant with the splitting, excitation from $m_s = 0$ to $m_s = \pm 1$ occurs, resulting in a reduction of fluorescence intensity. The degeneracy of the $m_s = \pm 1$ states was lifted with a static magnetic field that shifted the resonances symmetrically around the zero field splitting at 2.87 GHz. Even at zero magnetic field there can be a splitting due to strain in the nano diamond. In this case the additional splitting is important to determine the exact resonance frequency for the following coherent spin manipulation experiments.

3.5 Timing of the Sequences

An exact timing of the channels for MW, phase shifter, laser and APD gates is crucial for coherent spin manipulation described in section 3.6. The sequences for the channels are generated with the BPG. From the moment of

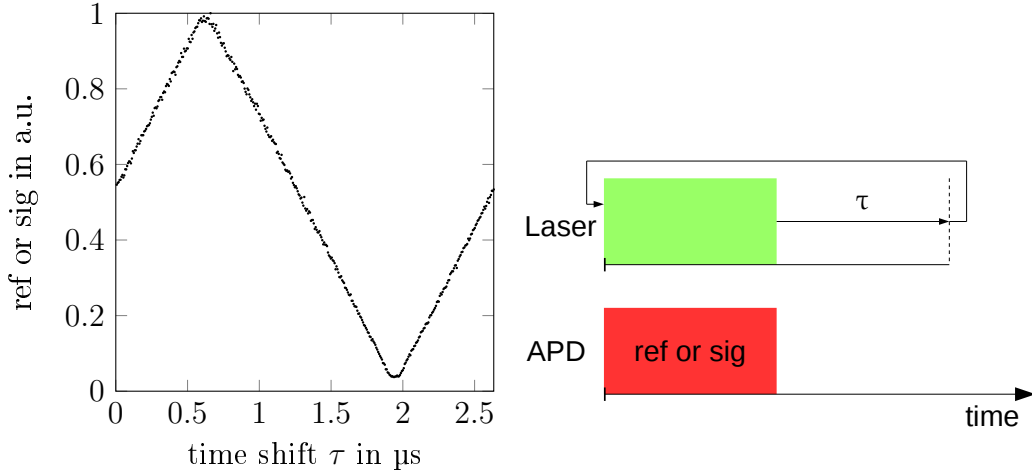


Figure 10: Measurement scheme and resulting signal for the timing of the gates. The gates are timed correctly relative to the laser if the maximum is at $\tau = 0$

programming the bit pattern, until these signals have effect on the experiment, there are time delays that differ for all channels. The differences of the delays are critical for pulse sequences with an accuracy of 6.7 ns and in the following it is described how to measure and correct them. Since absolute delays are irrelevant, the delay of one channel is set to zero, and the others are measured relatively to it. Finally, the channels are time shifted by the measured delay time to compensate it.

Experimentally it is the easiest way to set the delay of the laser to zero and to measure the others relatively to it, first the APD gates, then the MW switch and finally the phase shifter.

The results and the errors for the delays relative to the laser delay can be read out from the plots that are described in the following:

channel	reference gate	signal gate	microwave	phase shift
delay in μs	0.67 ± 0.03	0.60 ± 0.03	1.70 ± 0.05	1.93 ± 0.07

Delay of the APD Gates

A possible measurement scheme is shown in Fig. 10. Laser and APD gate are turned on for the first half of the sequence and turned off for the second.

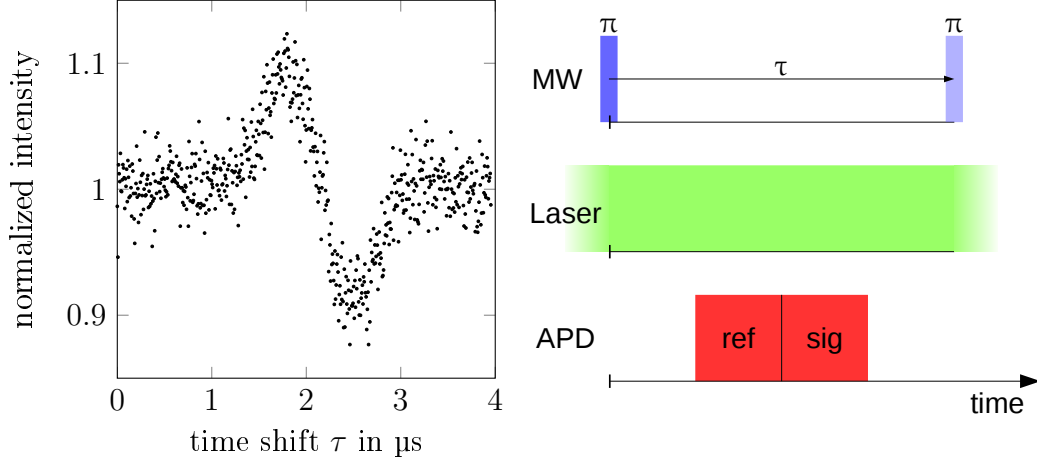


Figure 11: Measurement scheme and resulting signal for the timing of the MW. A π pulse is shifted through the sequence. This causes a peak followed by a dip, which are symmetrically around $\frac{1}{2}\tau_{\text{max}}$ if the MW is timed.

The sequence is repeated while the laser pulse is stepwise shifted by the time τ relative to the gate until it reaches its initial state at $\tau = \tau_{\text{max}}$. As the laser and the gate pulse overlap the intensity increases. For this sequence the recorded intensity as a function of the time shift τ results in a triangular function with the period τ_{max} . The gates are timed correctly if the maximum is at $\tau = 0$. The timing works the same for both gates but the delay can differ.

Delay of the MW

A convenient measurement scheme is shown in Fig. 11. The MW, resonant to the splitting between $m_s = 0$ and $m_s = \pm 1$, is turned on for the time π/Ω , where Ω is the Rabi frequency. If the system is initialized to the “bright” state $m_s = 0$ this π pulse converts the system to the “dark” state $m_s = \pm 1$. The laser is continuously turned on whereas the APD gates are partially turned on. The signal gate is turned on just as long as the reference gate and begins where the reference ends. The sequence is repeated while the π pulse is stepwise shifted by the time τ until it reaches its initial position at $\tau = \tau_{\text{max}}$. Reference and signal are detected as a function of the time shift τ . As the π

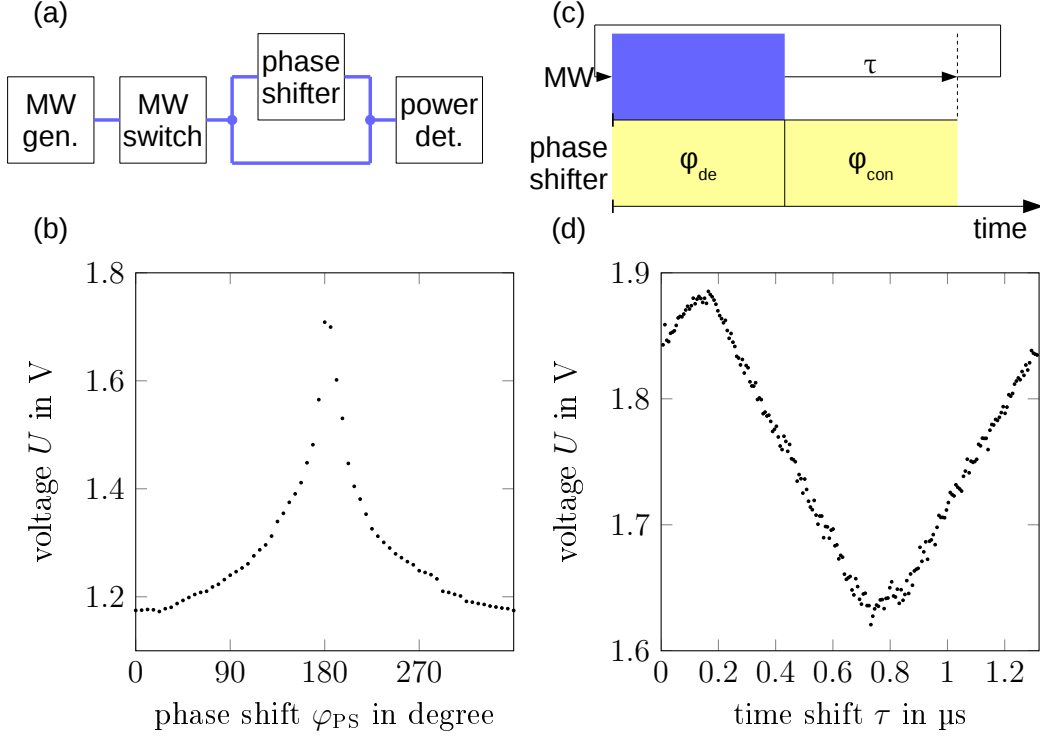


Figure 12: (a) “MW interferometer” and (b) interference signal. (c) Measurement scheme for the timing of the phase shifter relative to the MW and (d) the resulting signal.

pulse overlaps with the detection, the corresponding intensity decreases. In the normalized intensity (sig/ref) this results in a peak followed by a dip. The MW is timed correctly if peak and dip are symmetrically around $\frac{1}{2}\tau_{\text{max}}$. The resonance frequency was determined with an ODMR scan (section 3.4) and the π pulse length was determined by driving Rabi oscillations (section 3.6.1).

Delay of the Phase Shift

For this timing an “MW interferometer”, where one arm is phase shifted but the other not, is built up (Fig. 12a). The phase difference φ is composed of the phase shift due to the phase shifter $\varphi = \varphi_{PS}$ and an additional one due to different cable lengths φ_0 : $\varphi = \varphi_{PS} + \varphi_0$. If the two waves have the same

amplitude, the power P of the interfering waves is given by

$$P \propto \cos^2\left(\frac{\varphi}{2}\right). \quad (47)$$

The signal is analysed with an MW power detector. Its output is a DC voltage U that is proportional to the power level L_P of the incoming MW

$$U = c \cdot L_P \quad \text{with} \quad L_P = \log_{10}\left(\frac{P}{1 \text{ mW}}\right) \text{ dBm}, \quad (48)$$

where the proportionality constant c for the specific power detector and MW frequency is $c \approx -25 \text{ mV dBm}^{-1}$. Substitution of eq. 47 into eq. 48 gives the expected DC voltage

$$U \propto \log_{10}\left(\cos^2\left(\frac{\varphi}{2}\right)\right). \quad (49)$$

Fig. 12b shows the measured voltage as a function of the phase shift φ_{PS} which is in agreement with eq. 49. Destructive interference results in a sharp maximum and the corresponding phase shift φ_{de} can be read out from the plot. The phase shift for constructive interference is simply $\varphi_{\text{con}} = \varphi_{\text{de}} + 180^\circ$. Next, the following sequence is run (Fig. 12c): For the first half of the sequence the phase shifter is set to φ_{de} and the MW is turned on. For the second half the phase shifter is set to φ_{con} and the MW is turned off. The sequence is repeated and the MW pulse is stepwise shifted by the time τ until it reaches its initial position at $\tau = \tau_{\text{max}}$. Fig. 12d shows the measured voltage as a function of the time shift τ , which is a triangular function with a period of τ_{max} . The phase shift is timed correctly if the maximum is at $\tau = 0$.

3.6 Coherent Spin Manipulation

In this section the results of coherent spin manipulation, including Rabi oscillations and spin echo decays in the CPMG experiment, are presented. The measurement schemes (Fig. 13 and 14) are equal except from the MW sequence. The laser initializes the system to $|0\rangle$ while the reference is detected. Then everything is turned off for a few lifetimes of the metastable $|s\rangle$ state, which is indicated by “wait”, so that the system relaxes to $|g, m_s = 0\rangle$. Next, the MW sequence is run while laser and APD are turned off. After the MW sequence, laser and signal gate are turned on to read out the fluorescence.

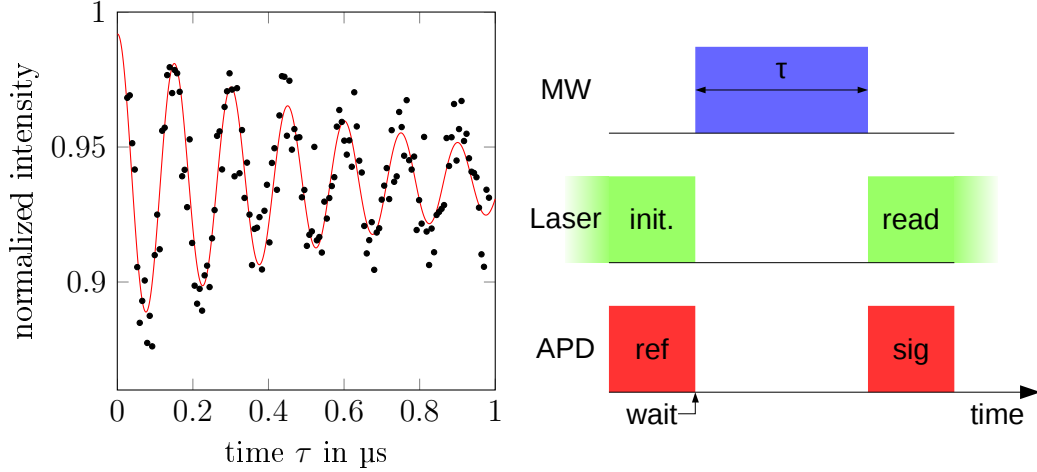


Figure 13: (left) Rabi oscillations. The MW power was set to 9 dBm at the MW generator. (right) The corresponding measurement scheme.

3.6.1 Rabi Oscillations

The simplest coherent spin manipulation is driving Rabi oscillations. After the initialization the microwave pulse is applied for the time τ and finally the spin state is read out. Applying a compensation pulse after the actual sequence for the time $\tau_{\text{max}} - \tau$ (which is not shown in the measurement scheme for clarity) keeps the total MW duration constant to avoid thermal drift of the NV center. Repeating this sequence while stepwise increasing τ results in the average fluorescence intensity of the spin state superposition which oscillates according to the Rabi oscillations performed by the system. Fig. 13 shows the measurement scheme and the resulting signal. According to eq. 37 the intensity can be described by

$$I_{\text{Rabi}}(\tau) = a \cdot \rho_{11}(\tau + \tau_0) + b \quad (50)$$

where a , b and τ_0 are fit parameters to adapt the theory to the experimental conditions. The results for the data shown in Fig. 13 are:

Ω in MHz	γ_2 in MHz	a	b	τ_0 in μs
41.9 ± 0.2	1.0 ± 0.1	0.9365 ± 0.0009	0.0021 ± 0.0001	0.110 ± 0.002

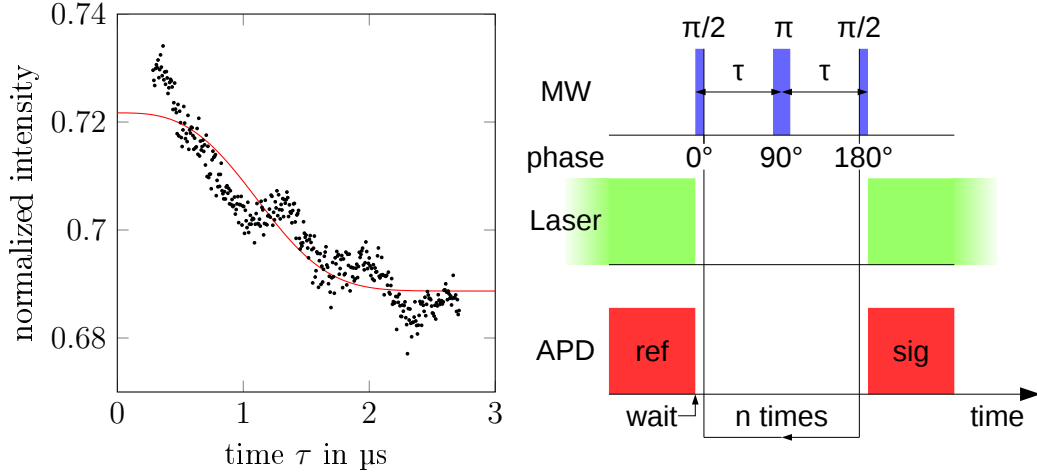


Figure 14: (left) Spin echo decay for the CPMG sequence with $n = 1$ and the following parameters: MW power at the MW generator 7 dBm, π pulse length 79.2 ns and integration time per point 116 s. (right) The corresponding measurement scheme.

3.6.2 CPMG Experiment

Since the Rabi frequency is determined, now the CPMG sequence can be performed. After the initialization the CPMG sequence (see section 2.4) is applied and finally the spin state is read out. Repeating this sequence while stepwise increasing τ results in the average fluorescence intensity of the spin echo state which decays exponentially. According to eq. 46 the intensity can be described by

$$I_{\text{CPMG}}(\tau) = a \cdot \exp\left(-\frac{2n\tau}{T_2} \left(\frac{2\tau}{T_2}\right)^2\right) + b, \quad (51)$$

where a and b are fit parameters that are introduced to adapt the theory to experimental conditions. The results for the data shown in Fig. 14 are:

T_2 in μs	a	b
2.54 ± 0.09	0.033 ± 0.001	0.6887 ± 0.00008

It was not demonstrated yet that the coherence time is prolonged for $n > 1$. The reasons for that are discussed in the upcoming conclusion.

4 Conclusion and Outlook

During the course of this work the CPMG sequence was successfully implemented, including the integration of the phase shifter. Further emphasis was put on the development of systematic methods for the timing of spin manipulation, optical excitation and photon detection (section 3.5). Software modifications were evolved to optimize and automate the experimental workflow. Once a single NV center is found on the sample, the whole spin manipulation process including ODMR, Rabi oscillations and the CPMG experiment, can be performed automatically. A first result of the spin echo decay with the CPMG sequence with one π pulse, which is effectively the Hahn echo sequence, was shown in Fig. 14.

The coherence time was measured to be $T_2 = (2.54 \pm 0.09) \mu\text{s}$. For more than one π pulse, T_2 is expected to be prolonged. The measurements to demonstrate that are currently in progress and could not be included in this thesis. It was already demonstrated by B. Naydenov et al. [23] for single NV centers in nano diamond where T_2 was prolonged from 2.1 μs with the Hahn echo sequence to 4.8 μs with the CPMG sequence.

There were unexpected oscillations in the spin echo decay (Fig. 14). These oscillations were just detected on the reference which indicates technical reasons.

Another technical problem to overcome is that the BPG crashes when it is programmed with long sequences. As a consequence it was not possible to perform the CPMG sequence with many π pulses yet.

One improvement of the setup in the near future will be the integration of

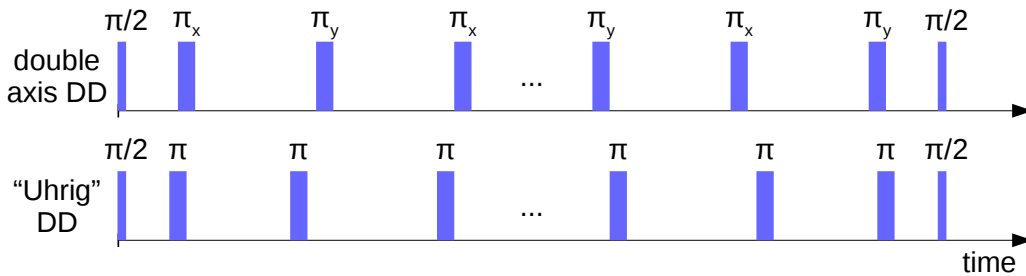


Figure 15: Dynamical decoupling protocols based on the CPMG sequence.

the MW switch, the phase shifter and the output ports of the BPG onto one PCB. Thus the setup will be clearly arranged and switching times and insertion loss will be reduced.

The systematic methods for the timing (section 3.5) can simply be used for a new integrated MW setup.

There are other dynamical decoupling (DD) protocols (Fig. 15) based on the CPMG sequence that can be more effective [24, 25]. In double-axis DD the rotation axis (blue vector in Fig. 5) points alternately in the x and y direction for each π pulse. In “Uhrig” DD, a better decoupling from the environment is reached by unequal spacings between the π pulses [26]. A combination of both sequences is also possible [24].

There are multiple applications of the NV center in quantum information processing [4, 5] and nanoscale electric and magnetic sensing [6–10] in which the CPMG sequence can improve the performance.

A List of Devices

Acousto-optic modulator AA Opto Electronic MT110-A1-VIS (modulator) and MODA110-B4500-30 (frequency driver with integrated amplifier and switch)

Avalanche photo diode Laser-Components Count 20-C, dark count rate 20 s^{-1} , photon detection efficiency ca. 0.7, dead time 45 ns

Bit pattern generator DEDITEC USB-BITP-200, time step 6.6 ns

Camera Hamamatsu ORCA-HR-C4742-85

Correlator PicoQuant TimeHarp 260, time correlated single photon counting (TCSPC), time resolution 25 ps, dead time $< 25\text{ ns}$

Laser Shanghai Laser & Optics Century GL532T3-200, diode pumped solid state laser (DPSSL), wavelength 632 nm, power 200 mW

Microwave amplifier Mini-Circuits ZHL-16W-43-S+, max. power 16 W

Microwave generator Agilent Technologies E8257D, power -20 dBm to 12 dBm , frequency 250 kHz to 31.8 GHz

Microwave power detector Mini-Circuits ZX47-40-S+

Microwave switch Mini-Circuits ZFSWA2-63DR+, switching time 35 ns

Phase shifter United Monolithic Semiconductors (UMS) CHP4012-QEG, surface-mount device (SMD), phase shift step 6.25° , switching time 15 ns

Objective Nikon CFI Plan Apo VC 100X Oil, numerical aperture 1.4, magnification $100\times$

Oscilloscope Tektronix MSO2024B

Piezo system piezosystem jena 92652 (xy direction), 70504 (z direction) and NV40 3CLE (controller)

Spectrometer Acton SpectraPro-500i, focal length 500 mm

B List of Abbreviations

AOM	acousto-optic modulator
APD	avalanche photo diode
BPG	bit pattern generator
BS	beam splitter
CPMG	Carr-Purcell-Meiboom-Gill (sequence)
DD	dynamical decoupling
DM	dichroic mirror
DPSSL	diode pumped solid state laser
EPR	electron paramagnetic resonance
HBT	Hanbury Brown and Twiss (effect)
LP	long pass filter
MW	microwave
NA	numerical aperture
NMR	nuclear magnetic resonance
NV	nitrogen vacancy (center)
OBE	optical Bloch equations
ODMR	optically detected magnetic resonance
PCB	printed circuit board
QIP	quantum information processing
RWA	rotating wave approximation
SF	spatial filter
SM	scanning mirror
SMF	single mode fibre
TCSPC	time-correlated single photon counting

References

- [1] C. Kurtsiefer et al. Stable solid-state source of single photons. *Physical Review Letters*, 85(2):290–293, 2000.
- [2] A. Gruber et al. Scanning confocal optical microscopy and magnetic resonance on single defect centers. *Science*, 276:2012–2014, 1997.
- [3] M. A. Nielsen and I. L. Chuang. *Quantum Computation and Quantum Information*. Cambridge University Press, 2000.
- [4] M. V. G. Dutt et al. Quantum register based on individual electronic and nuclear spin qubits in diamond. *Science*, 316:1312–1316, 2007.
- [5] P. Neumann. Quantum register based on coupled electron spins in a room-temperature solid. *Nature Physics*, 6:249–253, 2010.
- [6] G. Balasubramanian et al. Nanoscale imaging magnetometry with diamond spins under ambient conditions. *Nature*, 455:648–651, 2008.
- [7] J. R. Maze et al. Nanoscale magnetic sensing with an individual electronic spin in diamond. *Nature*, 455, 2008.
- [8] J. M. Taylor et al. High-sensitivity diamond magnetometer with nanoscale resolution. *Nature Physics*, 4:810–816, 2008.
- [9] C. L. Degen. Scanning magnetic field microscope with a diamond single-spin sensor. *Applied Physics Letters*, 92:243111, 2008.
- [10] F. Dolde et al. Electric-field sensing using single diamond spins. *Nature Physics*, 7:459–463, 2011.
- [11] AS. Barnard. Diamond standard in diagnostics: nanodiamond biolabels make their mark. *Analyst*, 134:1751–1764, 2009.
- [12] C. Kittel. *Introduction to Solid State Physics*. John Wiley & Sons, 8 edition, 2004.
- [13] Schirhagl et al. Nitrogen-vacancy centers in diamond: Nanoscale sensors for physics and biology. *Annual Review of Physical Chemistry*, 65, 2014.
- [14] R. Loudon. *The Quantum Theory of Light*. Oxford University Press, 3 edition, 2000.

- [15] H. J. Metcalf and P. van der Straaten. *Laser Cooling and Trapping*. Graduate Texts in Contemporary Physics. Springer-Verlag New York, 1999.
- [16] M. H. Levitt. *Spin Dynamics: Basics of Nuclear Magnetic Resonance*. John Wiley & Sons, 2 edition, 2008.
- [17] H. C. Torrey. Transient nutations in nuclear magnetic resonance. *Physical Review*, 76(8):1059, 1949.
- [18] L. Allen and J. H. Eberly. *Optical Resonance and Two-level Atoms*. Dover Publications, 1987.
- [19] E. L. Hahn. Spin echoes. *Physical Review*, 80:580, 1950.
- [20] H. Y. Carr and E. M. Purcell. Effects of diffusion on free precession in nuclear magnetic resonance experiments. *Physical Review*, 94:630, 1954.
- [21] S. Meiboom and D. Gill. Modified spin-echo method for measuring nuclear relaxation times. *Review of Scientific Instruments*, 29:688, 1958.
- [22] R. de Sousa. Electron spin as a spectrometer of nuclear-spin noise and other fluctuations. In M. Fanciulli, editor, *Electron Spin Resonance and Related Phenomena in Low-Dimensional Structures*, volume 115 of *Topics in Applied Physics*. Springer-Verlag, 2009.
- [23] B. Naydenov et al. Dynamical decoupling of a single-electron spin at room temperature. *Physical Review B*, 88:081201, 2011.
- [24] Z.-H. Wang et al. Comparison of dynamical decoupling protocols for a nitrogen-vacancy center in diamond. *Physical Review B*, 85:155204, 2012.
- [25] G. de Lange et al. Universal dynamical decoupling of a single solid-state spin from a spin bath. *Science*, 330:60–63, 2010.
- [26] G. Uhrig. Keeping a quantum bit alive by optimized π -pulse sequences. *Physical Review Letters*, 98:100504, 2007.

Danksagung

An dieser Stelle möchte ich allen danken, die mich unterstützt haben und damit diese Arbeit erst möglich gemacht haben.

Als erstes danke ich Prof. Dr. Oliver Benson und Prof. Dr. Kurt Busch für die Betreuung dieser Arbeit.

Weiterhin danke ich Bernd Sontheimer und Niko Nikolay für die großartige Unterstützung. Ich habe in der Zeit viel von euch gelernt.

Der gesamten Nanooptik-Gruppe danke ich für die tolle Atmosphäre. Ich habe mich hier sehr wohlfühlt.

Ein besonderer Dank gilt Andreas, Milan und Maria für ihre hilfreichen Korrekturen und Anmerkungen sowie die tolle mentale Unterstützung.

Selbstständigkeitserklärung

Hiermit versichere ich, dass ich die vorliegende Arbeit selbständig verfasst und keine anderen als die angegebenen Quellen und Hilfsmittel verwendet habe.

Berlin, den 22.02.2016

Fabian Loth